

# 3D RECONSTRUCTION SYSTEM BY MEANS OF UNIQUE CAMERA, STRUCTURED LIGHT AND MATHEMATICAL MODELS

**Elisângela Ribeiro**

Federal University of Lavras, School of Engineering, Lavras MG 37.200-900 Brazil

**Fernando Pujaico Rivera**

Federal University of Lavras, School of Engineering, Lavras MG 37.200-900 Brazil

**Bianca Batista Barreto**

Federal University of Lavras, School of Engineering, Lavras MG 37.200-900 Brazil

**Roberto Alves Braga Junior**

Federal University of Lavras, School of Engineering, Lavras MG 37.200-900 Brazil

**Marco Antônio Barbosa**

Federal University of Lavras, Faculty of Health Science, Lavras MG 37.200-900 Brazil

**Abstract:** 3D digital profiles are key information in many areas of knowledge, from medical to agricultural or industry. And in order to achieve reliable digitized surfaces we can have in hand techniques using laser, digital cameras, structured light associated to image processing tools. To choose the best technique we face some challenges based on the application itself, but on the cost of equipment, on the robustness and on the computational cost and programming complexity. This work aimed to address a reliable, robust and accessible methodology using just one camera and a light projector to, with mathematical models, generate digital 3D surfaces. The mathematical model was designed using the geometry of the system (camera, projector and object) with additional routine to adjust the optimum values of the variables involved. We validated the proposed method with known objects and presented a 3D reconstruction of objects that are difficult to achieve manually, such as a callote and the back of human-being. The results showed that the mathematical model created conditions to provide reliable outcomes from a low cost devices (webcam and regular light projector) usage, with correction of warping caused by perspective.

**Index terms:** Structured light; 3D profile; monocular vision.

Received: January 31, 2023 - Accepted: March 30, 2023

---

## INTRODUCTION

Regarding the relevance of 3D models in many applications we can see in recent days the improvement of methods to digitize objects alternatively to laser scanning, that has been considered as a gold standard (XU et al., 2019). The efficiency of laser scanning in 3D reconstruction is recognized in objects and scenes, though with concerns regarding its absolute cost or the price-quality balance (XU et al., 2019).

Therefore, in order to achieve similar results

using accessible systems one can observe movements towards the test of new devices such like RGB-D cameras (XU et al., 2019) and DLP projectors (ZHANG, B. et al., 2022) or even using approaches of image processing aided by neural network (ZHANG, B. et al., 2022)(YAO; GAI; DA, 2021).

The evaluation of the efficiency and high costs of multi-camera systems must be also considered (ZHANG, F. et al., 2022) since the adoption of single camera can reduce the price and the computational cost of a 3D reconstruction system

(XU et al., 2019). The adoption of single camera demands additional work such like phase-shift or the association of single-shot approaches with neural networks (ZHANG, B. et al., 2022) (WANG et al., 2019).

Despite all efforts one can observe room for improvements linking the robustness and low costs of using single camera with the advantages of modelling.

Three-dimensional modelling is the geometrical representation of an object inside the  $x$ ,  $y$ ,  $z$  planes (HWANG; KIM, 2013). Mathematical models are used to identify a specific model which best describes the form and dimensions of an object (HEIKKINEN; SCHAJER, 2020). The representation of objects through geometrical modelling have replaced with significant advantage real measurements, since it provides an analytical or mathematical description of the object being analyzed, moreover when the object has a complex shape to be reproduced by manual measurements. Thus, it is generally more convenient to perform tests and experiments with a model than with a real object. In addition to the analytical advantages, a model is a useful and necessary medium, in order to transmit and share data regarding the objects being analyzed.

One of the ways used to obtain a 3D reconstruction is through structured light. This is a technique where a pattern of light is projected on the surface of the object being modelled and a sensor is employed to capture an image of the object subjected to the projected patterns (KOKUBUM; TOMMASELLI; REISS, 2005). The construction of a 3D model may be obtained through the geometry between the sensor (the observer) and the projected beam of light from a known source, which can be either a regular projector or a laser line. These systems capture parts of the surface of an object and the pattern of light must be projected throughout all its area, in order to obtain a complete 3D model. Mathematical models are used in these systems to reconstruct and model the surface.

For instance, this method is present in the work of Barreto et al. (BARRETO et al., 2023), and it details the development of a low-cost

equipment: portable, robust and designed to characterize roughness and the presence of crust at the soil surface through a laser line and a monocular vision. Structured light and monocular vision was adopted by Coelho, Ribeiro, and Braga (COELHO; RIBEIRO; JUNIOR, 2019) with unwarping function to investigate the effects tractor tires would cause in agricultural areas by means of 3D reconstruction. That profilometrical method was also applied to estimate the surface area of poultry (SILVA et al., 2011), to measure the volume of oil in fruits (COSTA et al., 2016), to measure the surface profile of mechanical prototypes (GOMES et al., 2009), all of them aiming at low costs and flexibility, and it was also applied in postural analysis of human beings (FERNANDES et al., 2003).

Therefore, monocular structured light vision has proven to be a viable method to develop technologies which will enable to get the three-dimensional models of a wide range of objects accessibly without sacrificing sensibility. However, the use of only one sensor (camera) can compromise the 3D reconstruction, and the limitation caused by the perspective can be overcome by means of unwarping function (COELHO; RIBEIRO; JUNIOR, 2019) without the advantages presented by a mathematical model.

This work aimed to create a reliable, robust and accessible methodology to achieve 3D reconstruction by means of a monocular observer (camera), a regular light projector and a mathematical model based on geometrical features.

This article is divided as it follows: Section 2 is dedicated to the materials used and methods employed, divided in five subtopics. The first one describes the process of assembly of the experimental setup; the second subtopic details the method employed to digitize the surface to be analyzed, and the third describes how the binarization of a colored image is performed. The fourth subtopic illustrates the process of how a three-dimensional line is obtained from a 2D image, and finally, the last subtopic presents the procedure used to attain and optimize the parameters of the model being proposed. The

proposed methodology was tested in random surfaces with complex profile such as a callote and human-being's back. In section 3 results will be put forth along with discussions regarding them and in Section 4 conclusions are presented.

## MATERIAL AND METHODS

The methodology employed steps are listed as it follows:

- Experimental configuration proposed;
- Digitization of a known surface to obtain the model based on the setup;
- Binarizing colored image;
- Obtention of a 3D line from 2D images;
- Experimental optimization of the values according to the parameters of the model;
- Application in random surfaces.

### Experimental configuration

A projector – non-coherent light source – was associated with a digital camera (webcam) and both positioned in front of the object upon a reference surface, as illustrated in Figure 1.

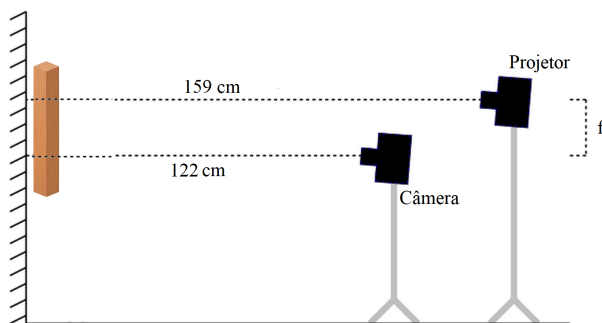


**Figure 1:** Experimental configuration of 3D reconstruction using structured light and a single camera.

The technical specifications of the devices are a webcam Logitech Hd, 3.0 Mb, Usb C270 960-000691; a Benq multimedia projector Mx525b

3200 Lumens/Xga/Hdmi/3D Ready/Bndes and a Sony Vaio Core i3. portable computer.

With the completion of the setup assembly, it was possible to identify the variables of the system as illustrated in Figure 2. Where:

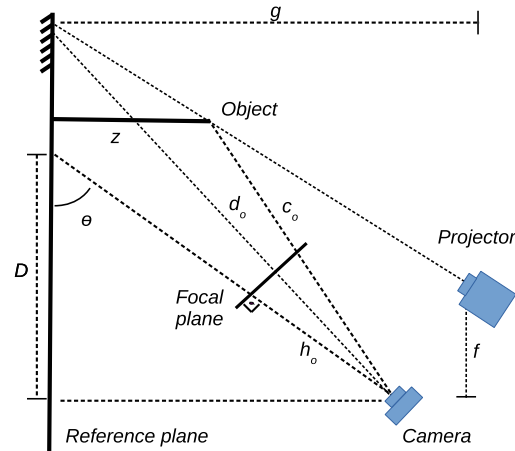


**Figure 2:** Top view of the experimental setup with the variables used in the model.

- $g$ : The distance (cm) of the projector in relation to the reference plane in centimeters;
- $f$ : The distance in centimeters (cm) between the projector and the camera;
- $\theta$ : The angle between the camera and the reference plane;
- $h_0$ : The Focal length of the camera measured in pixels;
- $D$ : The distance in centimeters (cm) between the camera's central line of sight and the camera's projecting line in the reference plane;
- $z$ : The object's real height (cm).
- $c_0$ : Relative height of the object in relation to  $d_0$  (line of reference);
- $d_0$ : Difference in pixels between the image's central point and the projected reference line observed within the plane of the digitized picture (Focal Plane).

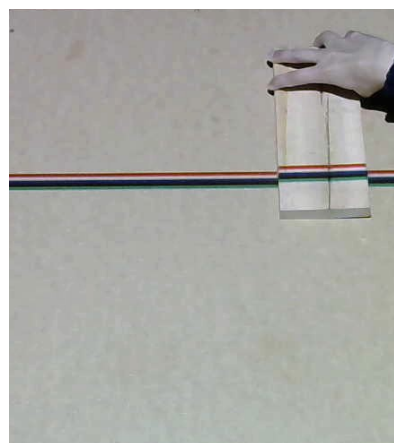
Initially, the variables  $D$ ,  $f$ ,  $g$  were manually measured and the following values identified:  $D=51$  cm;  $f =33$ cm;  $g=159$  cm. The variable  $h_0=246.15$  cm is an approximate value which is intrinsic to the camera and calculated through the data regarding the opening angle and the picture size in pixels. The value of  $\theta$ , is equal to 1.17 rad, this is the angle observed between the camera and the reference plane. The values that were measured manually had an intrinsic error. Thus, the development of optimization algorithms to validate these measurement was carried out. The algorithm was constructed in the scientific programming language GNU Octave, that demands a regular computer to run.

### Digitization of a surface

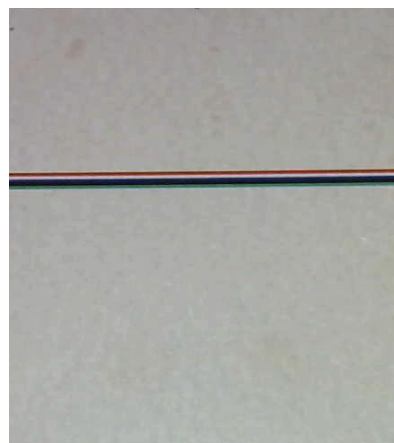
With the camera attached to a tripod, an image of the structured light line on the object's surface was captured, as illustrated in Figure 3a. Afterward, the object was removed, and the same procedure repeated. A new image was captured and defined as a reference image or line of reference, illustrated through Figure 3b.

Ambient light of the experimental setup is an important theme that ought to be addressed at this point. A multimedia projector is responsible for projecting the light patterns (lines) on the object's surface. The latter cannot be exposed to external light or direct sunlight and the ambient should be kept as dark as possible, so that only the projection of the lines (structured light) stand out. The darker the ambient the better the outline of the lines on the surface of the object is going to be. In other words, the contrast of the lines in the projection can be compromised by the external light. The user must bias the darkness regarding the power of the projector and the final result of the projected lines. The use of a line laser can be done to provide the lines, and can be more robust concerning the external light.

The lines used as projection consisted of five colors following the RGB pattern (LUKAC; PLATANIOTIS, 2005), forming a strip of red, white, blue, black, and green lines side by side. Thus, each line was one centimeter wide and disposed side by side, forming a strip with a width



(a)



(b)

**Figure 3:** Projection of the color lines (red, white, blue, black and green) side by side (a) on an object and (b) on a reference surface.

of five centimeters. The colors played a major role when identifying the profile of objects with different colors. Wooden samples were utilized to create our proposal had different shades and each one reflecting the light in a particular way. Thus, increasing the robustness of the technique for application in a large range of objects, for instance, in human bodies with multiple skin shades. An algorithm was developed to identify the best efficiency line according to the color of the object.

### Binarization of the colored image

The next step of the process is the image binarization choosing the color line with the best achievement to reproduce the surface's profile.

To carry out the process, an algorithm based on the identification of the colors of the lines was developed. When the line that best followed the object's profile was identified, the respective line remains, and the other lines discarded. Hence, a single line appeared in the final image of the digitized surface as illustrated in Figure 4. In the case of wooden samples, for instance, the red line had the best performance.



**Figure 4:** Image of  $D$  in black and white BW (binarized).

A given image  $\mathbf{A}$  with  $L$  pixels encoded in RGB, where  $a_l = (r_l, g_l, b_l) \in \mathbb{R}^3$  represents the pixel  $l$ ,  $\forall 1 \leq l \leq L$  in  $\mathbf{A}$ , so that  $r_l$  indicates the value of the pixel's red component,  $g_l$  indicates the value of the green component, and  $b_l$  the value of the blue component. We defined a color detector through the function  $f\_comp$  described in Equation (1),

$$f\_comp(\mathbf{a}, \mathbf{c}, \epsilon) = \begin{cases} 1 & \text{if } \frac{\|\mathbf{a}-\mathbf{c}\|}{\|\mathbf{c}\|} < |\epsilon|, \\ 0 & \text{else} \end{cases}, \quad (1)$$

Receiving as input the vectors  $\mathbf{a}$  and  $\mathbf{c}$  that represent the colors in the RGB format; the function then checks if these colors have a relative difference inferior to  $|\epsilon|$ , and if so, meaning that the vectors are slightly similar, thus, returning the value 1; and, if not, the value 0 is returned. In Equation (1) the operator  $\|\mathbf{c}\|$  indicates the Euclidean norm of  $\mathbf{c}$ . Therefore, to obtain the black

and white line, 4, from one of the lines projected in colors, it is used the function  $func\_compare()$ , so that a pixel of color  $\mathbf{a}_c$  is selected as a reference in the image  $\mathbf{A}$ , representing the color to be detected, and then compared with every pixel  $\mathbf{a}_l \in \mathbf{A}$ , achieving the result  $\mathbf{d}_l$ .

$$\mathbf{d}_l \leftarrow func\_compare(\mathbf{a}_l, \mathbf{a}_c, \epsilon), \quad \forall 1 \leq l \leq L; \quad (2)$$

The binary values of  $\mathbf{d}_l$  are then organized to form the image  $\mathbf{D}$ , as presented in Figure 4, where the white color represents the value 1(255) and the black color the value 0(0).

### Obtaining 3D line from 2D images

Using two binary images as a starting point – one of them presenting an object illuminated by lines with structured light and the other, with the same lines, illuminating a plane of reference (without the object) – we were able to obtain a 3D curve which represents the height of an object being studied in relation to the plane of reference.

This process is summarized in Figure 5a, where  $M$  points are extracted,  $p_m \in \mathbb{R}^3$  from the binary images (given in 2D) and converted to points  $P_m \in \mathbb{R}^3$  (in 3D), through the function  $func\_3d()$ , which receives the parameters of the model by the vector  $\mathbf{K} \equiv \{h_0, D, \theta, f, g\}$ ,

$$P \leftarrow func\_3d(p; \mathbf{K}), \quad (3)$$

$$p = (c_0, d_0, b_0) \xrightarrow[\mathbf{K}]{func\_3d} P(x, y, z), \quad (4)$$

$$p_m = (c_{0m}, d_{0m}, b_{0m}) \xrightarrow[\mathbf{K}]{func\_3d} P_m(x_m, y_m, z_m). \quad (5)$$

The points  $p_m$  are extracted from each column of binary images, and are referenced to the center of the image; it means that the values in  $p_m$  maybe positive or negative. Figure 5b shows how the values  $(b_0, c_0, d_0)$  are selected for a point  $p$ , highlighted with a red circle in the image. The center of the image is represented with a blue circle. The value  $d_0$  represents the vertical distance of a point belonging to the reference line to the

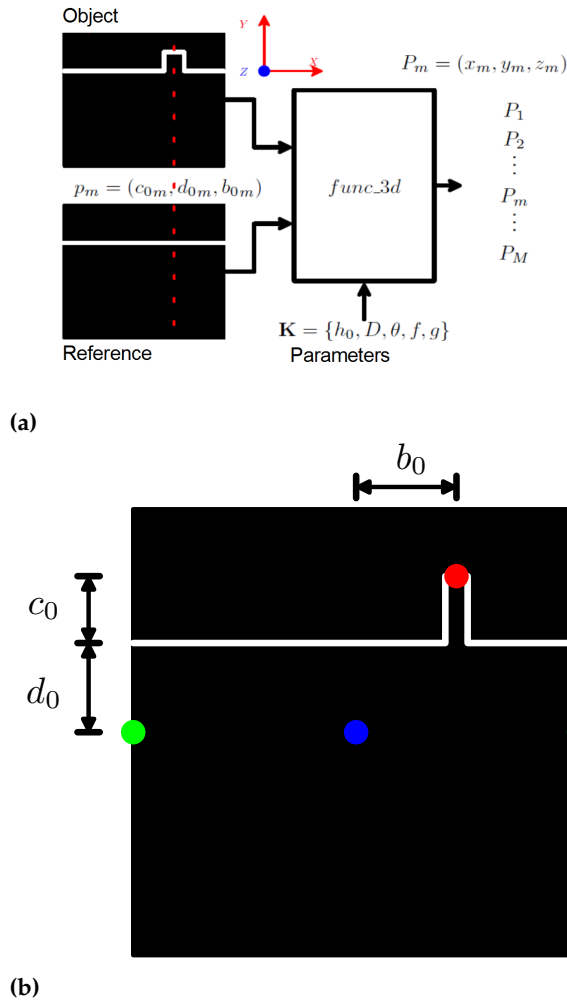


**Figure 5:** The inputs of the two images in the (a) block diagram to obtain (b) the parameters of the profile with a dot in blue representing the center of the image, the dots in green representing the border of the image in the center line and the dot in red representing the height of the object.

center of the image; the value  $c_0$  is the vertical distance of a point in the object's line to the reference line, and  $b_0$  the value of the horizontal distance of an object's line point to the center of the image.

The parameters in the vector  $\mathbf{K} \equiv \{h_0, D, \theta, f, g\}$  are extracted from the system's geometry, hence they're constant for every point  $p_m, \forall 1 \leq m \leq M$ . Figure 6 offers a top view of the system disposition, from where the variables  $h_0, D, \theta, f$  and  $g$  are obtained and the angles  $\gamma, \beta$  and  $\alpha$  as well as the values of  $y$  and  $z$  are presented, Figure 6a. Where  $z$  represents the height of the object

and  $y$  the vertical distance between the base of the object and the point in the reference plane where the camera is pointed to. The variable  $x$  is shown in Figure 6b and represents the distance of the object to the line of the central axis of the camera, this point  $P = (x, y, z)$  is  $(0, 0, 0)$  in 3D.

When analyzing the geometry described in Figure 6, we obtained mathematically the function  $func\_3d()$  which describes the height  $z$  of a point through the Equations (6) and (7),

$$z = \frac{D \operatorname{tg}(\theta) \left[ 1 + \operatorname{ctg} \left( \theta + \operatorname{atg} \left( \frac{h_0}{d_0 + c_0} \right) \right) \operatorname{ctg} \left( \theta - \operatorname{atg} \left( \frac{d_0}{h_0} \right) \right) \right]}{\left[ 1 + \operatorname{ctg} \left( \theta + \operatorname{atg} \left( \frac{h_0}{d_0 + c_0} \right) \right) \operatorname{ctg}(\alpha) \right]}, \quad (6)$$

$$\operatorname{ctg}(\alpha) = \frac{D \operatorname{tg}(\theta) \operatorname{ctg} \left( \theta - \operatorname{atg} \left( \frac{d_0}{h_0} \right) \right) - f}{g}. \quad (7)$$

The values  $x$  and  $y$  of a point being analyzed can be calculated using the following Equations (7) and (8),

$$y = D \operatorname{tg}(\theta) \operatorname{ctg} \left( \theta - \operatorname{atg} \left( \frac{d_0}{h_0} \right) \right) - D - z \operatorname{ctg}(\alpha). \quad (8)$$

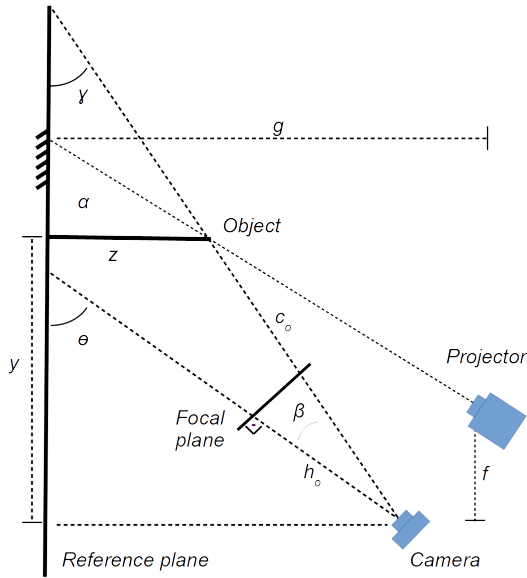
To achieve the value  $x$ , the angles  $\gamma$  and  $\beta$  were considered as demonstrated in Figure 6a. If we generate a segment with an angle  $\gamma$  in relation to the object and assuming that its longitude remains constant along the axis  $X$  for values of  $b_0$  next to the center, then, in the front view perspective, the variable  $x$  can be approximated as depicted in Figure 6b. Thus, we conclude that the variable  $x$  can be obtained from the Equations (9), (10) and (11), with the variables indicated in the Figure 6.

$$\gamma = \theta - \beta, \quad (9)$$

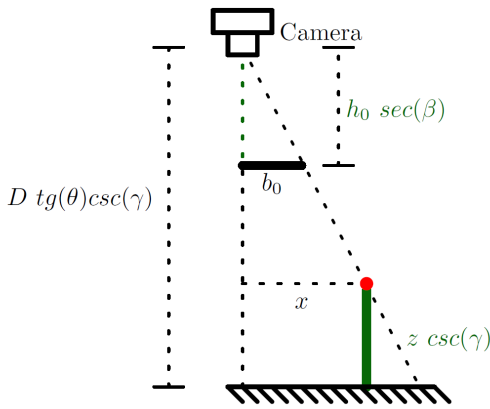
$$\beta = \operatorname{atg} \left( \frac{c_0 + d_0}{h_0} \right). \quad (10)$$

$$x = b_0 \left( \frac{D \operatorname{tg}(\theta) - z}{h_0} \right) \left( \frac{\operatorname{csc}(\gamma)}{\operatorname{sec}(\beta)} \right), \quad (11)$$

The procedure to obtains  $x$  allowed us to correct the warping caused by the perspective created by the angle of the camera and the projector.



(a)



(b)

**Figure 6:** Views from the setup with the variables used in the model, with (a) the sagittal view of the system locating the angles  $\alpha$  and  $\beta$  and (b) with the sagittal view regarding the camera disposition and the angle  $\gamma$ .

### Experimentally optimizing the accuracy of the parameters

In the system presented in Figure 7, the values of the parameters  $K = [h_0, D, \theta, f, g]$ , that were manually obtained and then optimized.

The system returns an optimized vector  $\mathbf{K}$  that generates the lowest error as possible when predicting

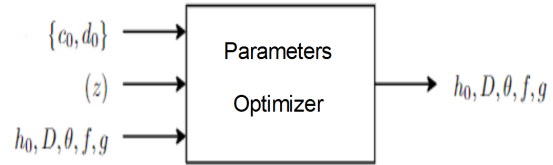


**Figure 7:** Optimizing the parameters of the image assembling system

the height  $z$  of the objects from the measures  $\{c_0, d_0\}$ . These variables can be seen in Figure 6. During the optimization process, the error  $E$  was added to the algorithm. It represents the value of the mean absolute error, estimated for the heights  $z$  in each of the interactions using the parameters  $[h_0, D, \theta, f, g]$ .

In order to achieve the best optimization results a regression was done over 52 values of the pair  $(\{c_0, d_0\}, \{z\})$ , which were ordered in blocks/vector. At this point, the greater the number of values  $(\{c_0, d_0\}, \{z\})$ , the better the adjustment of the parameters  $h_0, D, \theta, f$  and  $g$  are going to be. To obtain the pair  $(\{c_0, d_0\}, \{z\})$ , the digitization of four wooden samples with different heights was carried out, Figure 8.

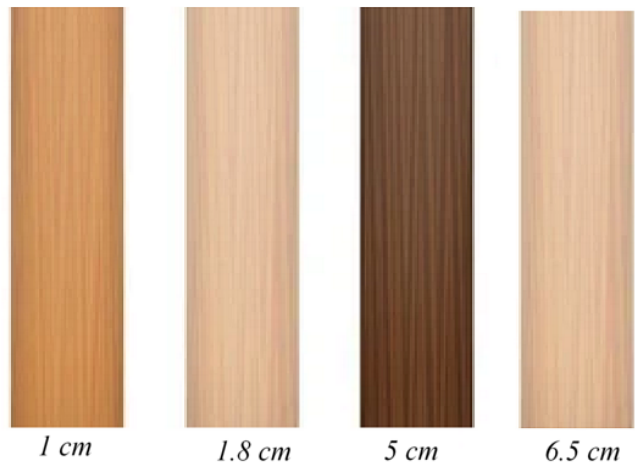


**Figure 8:** Four height values,  $z$ , of the wooden samples.

The wooden samples were digitized according to the experimental setup proposed, and during this process twelve lines were projected on each sample covering its surface.

The next step consisted of identifying the values of  $c_0, d_0$  for each line of the digitized wooden samples, and  $c_0$  was identified through the relative height in pixels of the object in relation to  $d_0$  (reference line) while  $d_0$  was identified through the difference in pixels between

the central point of the image and the projected line of reference.

In this way, in Figure 7, the input data to the optimization system were completed. And considered the approximated initial variables to  $h_0, D, \theta, f$  and  $g$ .

## Mathematical logic to parameters optimization

When obtaining a point  $P = (x, y, z)$  in 3D from the point  $p = (c_0, d_0, b_0)$  extracted using 2D images, we used the function  $P \leftarrow func\_3d(p; \mathbf{K})$ , being  $\mathbf{K} = [h_0, D, \theta, f, g]^T$  a vector containing the parameters of the system's geometry. Given that, the values in  $\mathbf{K} \in \mathbb{R}^5$  are manually measured initially and need to be adjusted into more realistic values, we can use the function  $func\_z()$  a simplification of the function  $func\_3d()$  when  $x = 0$  and  $y$  is discarded, where

$$z \leftarrow func\_z(\{c_0, d_0\}; \mathbf{K}), \quad (12)$$

$$\hat{p} = \{c_0, d_0\} \xrightarrow[\mathbf{K}]{func\_z} z; \quad (13)$$

so that the obtention of the height  $z$ , through the function  $func\_z()$ , depends exclusively of the values  $\hat{p} = \{c_0, d_0\}$  and  $\mathbf{K}$ , we used the function  $func\_z(\hat{p}; \mathbf{K}) \equiv z$  as described in Equation Eq. 6.

The binary images are obtained from the raw images of the known objects, obtaining  $L$  data  $\hat{p}_l$  and  $z_l, \forall 1 \leq l \leq L$ . Where  $z_l$  represents the height of the objects and  $\hat{p}_l$  are the data extracted from the objects in the binary images. The information stemming from the 3D and 2D scopes respectively, was defined the function of cost  $e(\mathbf{K})$ ,

$$e(\mathbf{K}) = \sum_{l=1}^L (z_l - func\_z(\hat{p}_l; \mathbf{K}))^2. \quad (14)$$

Thereby, if the values  $\mathbf{K}$ ,  $\hat{p}_l$  and  $z_l$ , are measured or obtained in an exact way,  $e(\mathbf{K})$  should be equal to zero, given that  $z_l \approx func\_z(\hat{p}_l; \mathbf{K})$ ; however, in practice we use approximated measurements; thus, our goal is to find the vector  $\mathbf{K} = \bar{\mathbf{K}}$  which minimizes  $e(\mathbf{K})$ .

To facilitate the obtaining of this minimum value (error), it is convenient to express the Equation (14) in a matrix form as in Equation (15)

$$e(\mathbf{K}) = \|\mathbf{Z} - \mathbf{F}(\mathbf{K})\|^2, \quad (15)$$

Where  $\mathbf{Z} \in \mathbb{R}^L$  is a column vector,  $\mathbf{F}(\mathbf{K}) : \mathbb{R}^5 \rightarrow \mathbb{R}^L$  is a vector-valued function, and its variable is represented by  $\mathbf{K}$ , and the operator  $\|\cdot\|^2$  indicates the square of the vector's norm,

$$\mathbf{Z} = \begin{bmatrix} z_1 \\ z_2 \\ \vdots \\ z_l \\ \vdots \\ z_L \end{bmatrix}, \quad \mathbf{F}(\mathbf{K}) = \begin{bmatrix} func\_z(\hat{p}_1; \mathbf{K}) \\ func\_z(\hat{p}_2; \mathbf{K}) \\ \vdots \\ func\_z(\hat{p}_l; \mathbf{K}) \\ \vdots \\ func\_z(\hat{p}_L; \mathbf{K}) \end{bmatrix}. \quad (16)$$

Thus, to minimize the Equation (15) we can apply the Algorithm of Levenberg-Marquardt (ALM), also known as the damped least-squares method (DLS) (DOICU; TRAUTMANN; SCHREIER, 2010, pp. 232-234) (PUJAICO RIVERA, 2020, pp. 82). So that the vector  $\bar{\mathbf{K}}$  that minimizes the Equation (15) is calculated iteratively using the Equation (17)

$$\mathbf{K}_{i+1} \leftarrow \mathbf{K}_i + \left[ \mathbf{J}(\mathbf{K}_i)^T \mathbf{J}(\mathbf{K}_i) + \alpha \mathbf{I} \right]^{-1} \mathbf{J}(\mathbf{K}_i)^T [\mathbf{Z} - \mathbf{F}(\mathbf{K}_i)], \quad (17)$$

Where  $\mathbf{I}$  is an identity matrix of  $5 \times 5$ , and the variable  $\alpha \geq 0$  is a chosen factor of regularization, in order to get a matrix  $[\mathbf{J}(\mathbf{K}_i)^T \mathbf{J}(\mathbf{K}_i) + \alpha \mathbf{I}]$  that always have its inverse form, and  $\mathbf{J}(\mathbf{K}) \in \mathbb{R}^{L \times 5}$  is a jacobian matrix (ZHANG, 2017, pp. 130) of  $\mathbf{F}(\mathbf{K})$ ; that is

$$\mathbf{J}(\mathbf{K}) = \frac{\partial \mathbf{F}(\mathbf{K})}{\partial \mathbf{K}^T} = \begin{bmatrix} \frac{\partial func\_z(\hat{p}_1; \mathbf{K})}{\partial \mathbf{K}^T} \\ \frac{\partial func\_z(\hat{p}_2; \mathbf{K})}{\partial \mathbf{K}^T} \\ \vdots \\ \frac{\partial func\_z(\hat{p}_L; \mathbf{K})}{\partial \mathbf{K}^T} \end{bmatrix}, \quad (18)$$

$$\frac{\partial func\_z(\hat{p}; \mathbf{K})}{\partial \mathbf{K}^T} \equiv \begin{bmatrix} \frac{\partial func\_z(\hat{p}; \mathbf{K})}{\partial h_0} \\ \frac{\partial func\_z(\hat{p}; \mathbf{K})}{\partial D} \\ \frac{\partial func\_z(\hat{p}; \mathbf{K})}{\partial \theta} \\ \frac{\partial func\_z(\hat{p}; \mathbf{K})}{\partial f} \\ \frac{\partial func\_z(\hat{p}; \mathbf{K})}{\partial g} \end{bmatrix}^T. \quad (19)$$

Finally, the Equation 17 converges to a vector  $\mathbf{K}_{i+1}$  which is a local minimum or global of  $e(\mathbf{K})$ ; if we initiate an iterative calculus from a value  $\mathbf{K}_0$  next to the solution, in this case the values  $\{h_0, D, \theta, f, g\}$  are used and they're either measured or mathematically obtained.

The iterations cease when  $\mathbf{K}_{i+1} \approx \mathbf{K}_i$  where is declared the optimal value  $\bar{\mathbf{K}} \equiv \mathbf{K}_{i+1}$ .

## Application on random surfaces

The method after calibration, was tested on random surfaces, that is, on surfaces where the 3D model is a real challenge without digital scanning. The first

sample used was a calotte with known  $Z$  value of 10 cm, and the second was the human body's back surface.

The validation of the 3D reconstruction of the human body's back surface was carried out by addressing postural classifications in the digital model compared with the real specimen (human-being) provided by an expert.

### 3D reconstruction of a calotte

Figure 9 shows a round object being illuminated by a section of light generated by the projector.



**Figure 9:** Projection of the lines in the round object, callote.

Nine different lines were photographed on the object being digitized. Using only nine projected lines the model was obtained and a 3D surface generated after rendering the points using an interpolation.

### 3D reconstruction of human body's back

The work with humans was approved by the University's Human Research Ethics Committee. One volunteer had the postural classification as normal and another had the postural classification with left thoracic scoliosis in low level.

To provide the 3D reconstruction of a volunteer with normal posture 17 lines were projected using the same experimental configuration proposed. In the case of the volunteer that had a posture with scoliosis 19 lines were projected. The number of lines was chosen regarding the height of the volunteer.

## RESULTS AND DISCUSSIONS

### Optimization and validation using known samples

In Table 1 we can see the parameters obtained manually from the four known samples.

**Table 1:** Parameters identified manually in all four photographed samples, in centimeters.

$c_0$	$d_0$	$z$	$c_0$	$d_0$	$z$	$c_0$	$d_0$	$z$
3	0	1	5	-1	1.8	15	13	5
3	-11	1	7	-12	1.8	16	10	5
3	-16	1	5	50	1.8	17	2	5
3	43	1	4	46	1.8	17	0	5
2	38	1	6	40	1.8	16	-2	5
3	32	1	5	35	1.8	17	-6	5
1	26	1	5	27	1.8	16	-7	5
2	20	1	7	21	1.8	17	-10	5
1	15	1	6	17	1.8	16	-13	5
4	10	1	7	11	1.8	16	49	5
3	49	1	5	4	1.8	15	80	5
4	68	1	6	107	1.8	16	89	5
2	82	1	6	68	1.8	16	99	5
2	99	1	5	100	1.8	15	106	5
21	50	6.5	22	45	6.5	20	41	6.5
21	35	6.5	21	27	6.5	22	21	6.5
20	17	6.5	21	12	6.5	22	4	6.5
10	-2	6.5						

When processing the optimization algorithm using the data, the system returned an optimized vector  $\mathbf{K}$  with a mean error equal to 0.24 centimeters when predicting the height  $z$  of the four wooden samples with height from 1 to 6.5 cm. As to the variable  $D$ , a value of 49.02 cm was identified, as illustrated in 6a;  $\theta$  is equal to 0.93 radians, the angle formed by the camera on the plane; the distance between the projector and the camera is 31.06 centimeters, represented by the variable  $f$ ; the best parameter for the variable  $g$  was 161.94 centimeters, representing the height of the projector in relation to the reference plane. Table 2 lists the data manually measured and their optimized counterparts obtained through the optimization.

Using the optimized variables, these results of  $z$  presented an error of 0.24 cm to all cases. Once we have the parameters of the model optimized and validated using the wooden samples with known heights ( $Z$  values) with known and acceptable errors, we could generate 3D reconstruction from unknown surfaces or from surfaces that presents challenges to obtain their profile.

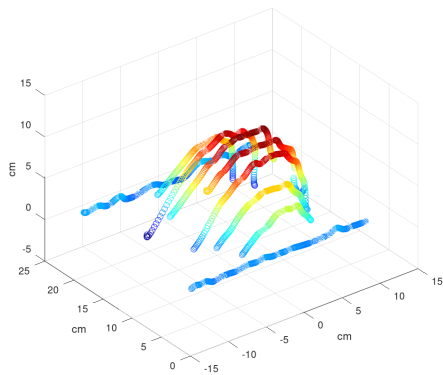
**Table 2:** Manually measured data x optimized data, in centimeters.

Variables	Manual	Optimized
$h_0$	246.15	248.59
D	51 cm	49.02 cm
$\theta$	1.17 rad	0.93 rad
f	33 cm	31.06 cm
g	159 cm	161.94 cm

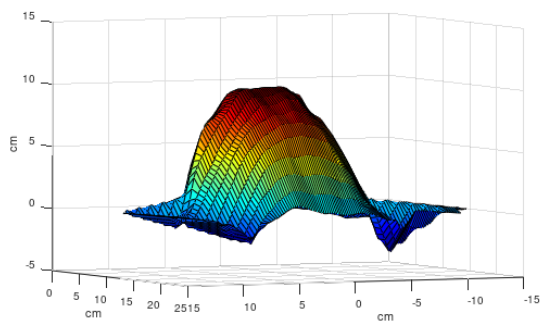
## Application on random surfaces

### 3D reconstruction of a calotte

We could do, using the same methodology, 3D reconstruction of a round surface different from the square and regular surfaces of wood. In Figure 10, it is shown, using the GNU Octave software, a three-dimensional object (a convex surface of a callote) with its dimensions along the axis presented by the profile of the callote at the nine lines projected (Figure 10a) or by the surface constructed after an interpolation and a rendering process. And it clearly demonstrates



(a)



(b)

**Figure 10:** 3D results of a calotte with (a) the profile of the lines and (b) the rendered surface.

the feasible of a 3D reconstruction from a round object using only nine lines. Moreover, an improvement can be made increasing the number of lines projected. The result shows the outcome of the modelling from the object accessed by an analytical description. The adoption of only one camera associated with a geometrical model has the advantage regarding the low cost and the robustness if compared to multi-camera approaches (ZHANG, F. et al., 2022) or laser scanning (XU et al., 2019). A 3D image offers to the users a better detailing of the object and a realistic digital vision of the same, as seen in Figure 10b, by which the user can access the object's height in different positions. Moreover, an accessible and low cost methodology can help many research laboratories, industries and other fields of applications to adopt the 3D reconstruction system. Figure 11 presents one profile isolated from the others to show the profile of one line, at cote 9 cm.

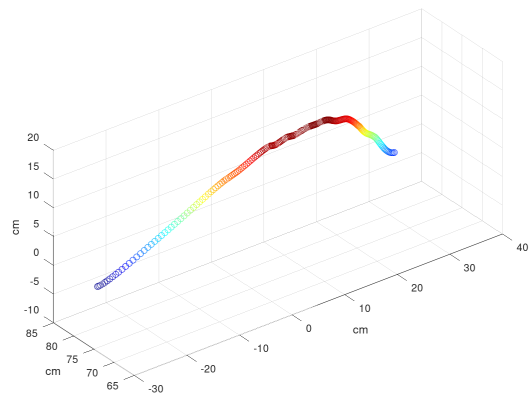


**Figure 11:** Plot of a profile of the calotte at cote 9 cm.

### 3D reconstruction of human body's back.

In Figure 12, we can observe the Illuminated back with normal posture of the spine, and in the Figure 13 the 3D reconstruction of a human body's back where the position is considered normal by an expert using the traditional approach to validate. The traditional judgement made by an expert in postural analysis was done aided by a physical grid placed between the person and the analyst himself, the symmetrograph. And using its intrinsic subjectivity and experience the process finishes with an error or misjudgment that can compromise the analysis. Thus, small sideways curve of the column can be neglected by the analyst.

While in Figure 14, we can observe the illuminated back with scoliosis in the spine, and in the Figure 15 the 3D reconstruction of a human body's back, classified by

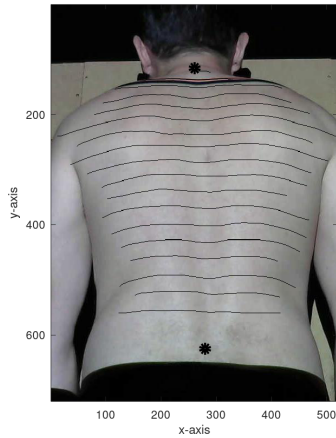
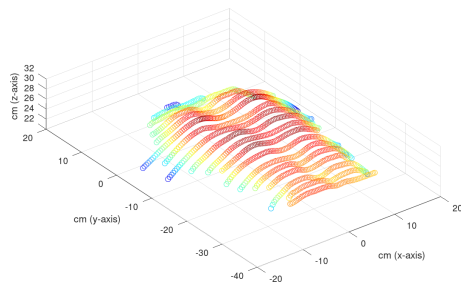
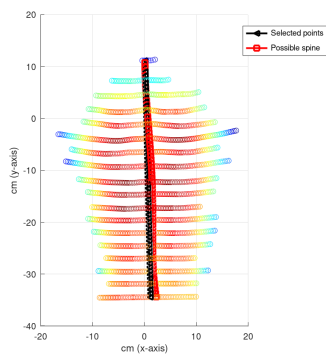


**Figure 12:** Human's back with normal posture and with the lines projected and the two references points.



(a)



(b)

**Figure 13:** 3D reconstruction of a human's back with (a) the 3D profile obtained using the methodology and (b) the comparison of the ideal center line (in black) of the spine with the center line obtained from the 3D profile (in red) indicating normal disposition of the spine with any sideways.

the analyst with low level of scoliosis, and confirmed by the sideways curve from the center line of the column in

the 3D image reconstructed (Figure 15 c). The curvature of the spine, measured in degrees.

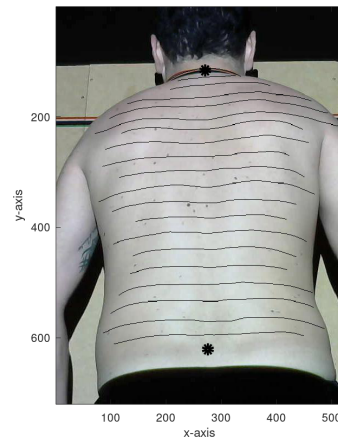


**Figure 14:** Human's back with scoliosis and with the projected lines.

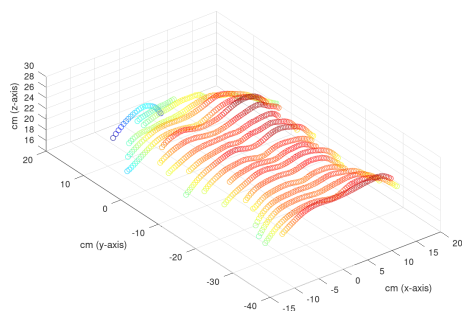
In the case, the level of scoliosis was moderate since the curve presented a curvature with angle smaller than 25 degrees. In the case of the real-time evaluation, by means of the symmetrograph, the level of curvature was observed subjectively; while in the case of the 3D image, the measure of the curvature can be done aided by the computer.

Therefore, one can see that the sensitivity of the methodology proposed is feasible to applications such as in human bodies modeling. In addition, as claimed before, the reliability of the mathematical models to create a 3D function that can be accessed quantitatively by the users was successfully achieved, in addition reducing the subjectivity of human evaluation, such as regarding the case of the postural studies.

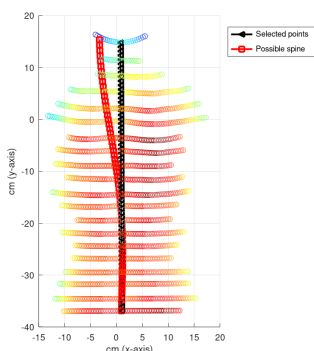
The 3D reconstruction of human bodies is a challenging process and the use of geometrical models presents reliable results such as using the Shape from shading (SFS) approach (JIN; AIMIN; JINGNAN, 2006).

Summary of the achievements:

- The geometrical model could be achieved using low cost devices;
- The geometrical model addressed reliable results for different objects;
- The adoption in human's back presented reliable results;
- The new steps are linked to test the model in a large number of samples.



(a)



(b)

**Figure 15:** 3D reconstruction of a human’s back with (a) the 3D profile obtained using the methodology and (b) the comparison of the ideal center line (in black) of the spine with the center line obtained from the 3D profile (in red) indicating the sideways curve of the spine due to scoliosis.

## ACKNOWLEDGEMENTS

This work received partial support from CNPq, Fapemig, Capes and UFLA.

## CONCLUSIONS

This work presented a mathematical model proposal intended to construct a system of digitization of objects that allows using 3D representation accessibly. It employed only one light source (accessible light projector) and only one observer (digital camera). In short, we presented the reliability to create an analytical model of unknown objects, and thus their 3D reconstruction. The variables of the model were optimized using known objects, particularly using their known heights, providing a fine calibration. Despite the limitation presented by the use of just one camera, the model developed could address the profile of unknown objects, as well as providing their 3D reconstruction

unwarping. The flexibility and the robustness of an analytical model offers possibility of many applications that does not demand expensive equipment and very detailed reconstruction. The results applied as a test in a callote and in a back of human-being reflecting the real surfaces respectively.

## REFERENCES

- BARRETO, Bianca Batista et al. Optical and portable equipment for characterizing soil roughness. **Smart Agricultural Technology**, Elsevier, v. 3, p. 100062, 2023. DOI: 10.1016/j.attech.2022.100062.
- COELHO, Diego Eduardo Costa; RIBEIRO, Elisângela; JUNIOR, Roberto Alves Braga. Development of an optical technique for scan the soil after the contact with wheels. **Theoretical and Applied Engineering**, v. 3, p. 3, 2019. DOI: 10.31422/taae.v3i3.16.
- COSTA, Anderson G et al. Measurement of volume of macaw palm fruit using traditional and the digital Moiré techniques. **Revista Brasileira de Engenharia Agrícola e Ambiental**, v. 20, p. 152–157, 2016. DOI: 10.1590/1807-1929/agriambi.v20n2p152-157.
- DOICU, A.; TRAUTMANN, T.; SCHREIER, F. **Numerical Regularization for Atmospheric Inverse Problems**. [S.l.]: Springer Berlin Heidelberg, 2010. (Springer Praxis Books). ISBN 9783642054396.
- FERNANDES, Luciane Fernanda Rodrigues Martinho et al. Utilização da técnica de Moiré para detectar alterações posturais. **Fisioterapia e Pesquisa**, v. 10, n. 1, p. 16–23, 2003. DOI: 10.1590/fpusp.v10i1.77507.
- GOMES, T. S. et al. Calibração da técnica de moiré aplicada a perfilometria de protótipos mecânicos. **Ciência e Agrotecnologia**, 33(2), p. 574–579, 2009. DOI: 10.1590/S1413-70542009000200033.
- HEIKKINEN, Juuso; SCHAJER, Gary S. A geometric model of surface motion measurement by objective speckle imaging. **Optics and Lasers in Engineering**, v. 124, n. 7, p. 105850, 2020. DOI: <https://doi.org/10.1016/j.optlaseng.2019.105850>.
- HWANG, Yong Seok; KIM, Eun-Soo. Perspective-variant reconstruction of a three-dimensional object along the depth direction with virtually generated elemental images by ray-based pixel mapping in integral-imaging. **Optics and Lasers in Engineering**, v. 51, n. 7, p. 797–807, 2013. DOI: 10.1016/j.optlaseng.2013.01.014.
- JIN, Li; AIMIN, Ren; JINGNAN, Zhang. 3D Reconstruction by Perspective Shape from Shading Using Linearized Triangular Element Surface Model. In: 2006 International Conference on Mechatronics and Automation. [S.l.: s.n.], 2006. P. 1763–1768. DOI: 10.1109/ICMA.2006.257481.

KOKUBUM, Christiane Nogueira de Carvalho;  
TOMMASELLI, Antonio Maria Garcia;  
REISS, Mário Luiz Lopes. Classificação automática de padrões projetados por um sistema de luz estruturada. **Bulletin of Geodetic Science**, v. 11, n. 1, p. 89–116, 2005.

LUKAC, Rastislav; PLATANIOTIS, Konstantinos N. Universal demosaicking for imaging pipelines with an RGB color filter array. **Pattern Recognition**, v. 38, n. 11, p. 2208–2212, 2005. DOI: 10.1016/j.patcog.2005.04.008.

PUJAICO RIVERA, Fernando. **Métodos numéricos: problemas não lineares e inversos**. 1ra. [S.l.: s.n.], Aug. 2020. ISBN 9786500073140. Available from: <<https://trucomanx.github.io/metodos.numericos/>>.

SILVA, Gleice C de A et al. Recuperação da topografia de ovos por meio da técnica de moiré e calibração independente. **Engenharia Agrícola**, SciELO Brasil, v. 31, p. 211–218, 2011. DOI: 10.1590/S0100-69162011000200001.

WANG, Y et al. Single-shot phase measuring profilometry based on color binary grating with intervals. **Optics Communications**, v. 451, p. 268–275, 2019. DOI: 10.1016/j.optcom.2019.06.062.

XU, Haonan et al. 3D reconstruction system for collaborative scanning based on multiple RGB-D cameras. **Pattern Recognition Letters**, v. 128, p. 505–512, 2019. DOI: 10.1016/j.patrec.2019.10.020.

YAO, P; GAI, S; DA, F. Coding-net: A multi-purpose neural network for fringe projection profilometry. **Optics Communications**, v. 489, p. 126887, 2021. DOI: 10.1016/j.optcom.2021.126887.

ZHANG, Bingwei et al. Single-shot high-precision 3D reconstruction with color fringe projection profilometry based BP neural network. **Optics Communications**, v. 517, p. 128323, 2022. DOI: 10.1016/j.optcom.2022.128323.

ZHANG, Fuhao et al. Three-dimensional reconstruction for flame chemiluminescence field using a calibration enhanced non-negative algebraic reconstruction technique. **Optics Communications**, v. 520, p. 128530, 2022. DOI: 10.1016/j.optcom.2022.128530.

ZHANG, X.D. **Matrix Analysis and Applications**. [S.l.]: Cambridge University Press, 2017. ISBN 9781108417419.